

Cite this article as: Huang Junyuan, Zhang Wei. Effect of Heat Treatment Duration on Corrosion Performance of Electron Beam Manufactured Ti6Al4V Alloy[J]. Rare Metal Materials and Engineering, 2024, 53(02): 357-364. DOI: 10.12442/j.issn.1002-185X.20230534.

ARTICLE

Effect of Heat Treatment Duration on Corrosion Performance of Electron Beam Manufactured Ti6Al4V Alloy

Huang Junyuan, Zhang Wei

School of Mechanical Engineering & Automation, Beihang University, Beijing 100191, China

Abstract: Ti6Al4V specimens prepared by electron beam selective melting were heat-treated for 1, 3, 5, 7, and 9 h, and the Tafel and electrochemical impedance spectroscopy experiments were conducted to discuss the behavior and mechanism of electrochemical corrosion. Through the modification mechanism analysis of corrosion performance, it is found that the more the $\langle 111 \rangle$ crystal orientations, the greater the proportion of small-angle grain boundaries, the larger the grain diameter, and the better the corrosion resistance. The specimen after heat treatment for 5 h has the most uniform $\langle 111 \rangle$ crystal orientations. The proportion of small-angle grain boundaries is the highest of 56.2%, the grain intercept is 5.252 μm , and the corrosion resistance is optimal with corrosion current of 0.037 $\mu\text{A}/\text{cm}^2$.

Key words: Ti6Al4V; electron beam selective melting; corrosion resistance; crystal phase; crystal structure

Titanium is an indispensable structural metal developed in the 1950s^[1-3]. Titanium alloys have high strength, good corrosion resistance, and non-toxic characteristic^[4-5], which can be used under harsh conditions, such as outer space, and can be safely implanted into human body^[6]. Ti6Al4V alloy has the advantages of both α and β titanium alloys, presenting high-temperature resistance and good seawater corrosion resistance^[7], which is widely used in biomedical and aerospace fields^[8].

Electron beam selective melting (EBSM) manufacturing technique uses the high-energy electron beams to selectively melt powder materials under high vacuum condition for rapid processing of pre-designed three-dimensional model^[9-10]. Compared with the traditional production techniques, EBSM has the advantages of fast processing speed and high productivity^[11-12], therefore attracting much attention^[13-14]. Knapp et al^[15] investigated the transient and spatial evolution of the fusion zone geometry, temperature gradient, and solidification growth rate during EBSM of powder bed. Lee et al^[16] compared the biomechanical performance of EBSMed and conventionally machined Ti6Al4V ELI screws. Montelione et al^[17] analyzed the EBSM powder particles after alpha-case heat treatment by the powder recovery system.

It is found that the materials processed by EBSM are prone to form cracks and pores, which degrades the performance of Ti6Al4V alloy^[18-21]. Qiu et al^[22] found that the Ti6Al4V alloy prepared by EBSM has worse corrosion resistance than those prepared by spark plasma sintering and selective laser melting techniques do. Chern et al^[23] reported that the hot isostatic pressing cannot improve the fatigue life of Ti6Al4V alloy prepared by EBSM. Xiu et al^[24] found that the EBSMed Ti6Al4V alloys after solution and aging treatments exhibit better mechanical properties and corrosion resistance than the commercial as-cast Ti6Al4V alloy does.

In this research, EBSM was used to prepare Ti6Al4V alloy, and the electrochemical corrosion performance and mechanism of EBSMed Ti6Al4V alloy after heat treatment for 1, 3, 5, 7, and 9 h were analyzed. The electrochemical corrosion performance of the specimen was studied by the Tafel and electrochemical impedance spectroscopy (EIS) experiments. The phases, internal defects, and grain diameters of the specimens were compared, and the effect and mechanism of the heat treatment on the corrosion performance were investigated, providing guidance to further improve the performance of alloys produced by EBSM.

Received date: August 30, 2023

Foundation item: National Natural Science Foundation of China (51975036)

Corresponding author: Zhang Wei, Ph. D., Professor, School of Mechanical Engineering & Automation, Beihang University, Beijing 100191, P. R. China, E-mail: zhangweibh@buaa.edu.cn

Copyright © 2024, Northwest Institute for Nonferrous Metal Research. Published by Science Press. All rights reserved.

1 Experiment

The additive manufacturing specimens were prepared by EBSM additive manufacturing equipment (Beihang University and the Astronautics and Aviation Industry Manufacturing Technology Research Institute). Ti6Al4V alloy powder was provided by AVIC Matt Additive Technology (Beijing) Co., Ltd. EBSM specimens were heat-treated in muffle furnace (SG-QF1400, Shanghai Sager Furnace Co., Ltd, China) for different durations. Firstly, the specimens were heated to 600 °C within 1 h. Then, they were kept at 600 °C for different durations (1, 3, 5, 7, and 9 h). Finally, the specimens were cooled in the furnace. The specimens after heat treatment for 1, 3, 5, 7, and 9 h were named as HT1, HT3, HT5, HT7, and HT9 specimens, respectively. After cooling process, the specimens were cut into small ones of 10 mm×10 mm×2 mm by wire electric discharge machine (MV series, Mitsubishi, Japan).

Before the corrosion test, the surfaces were polished by sandpaper from 300# to 1000#, rinsed, and soaked in polarized test environment. Electrochemical corrosion tester (Versastat 4 Potentiostat Galvanostat, AMETEK, USA) was used to obtain Tafel curves in the range from -1 V vs. SCE to 1.5 V vs. SCE when the open circuit potential was stable, and the scan rate was 1 mV/s. For EIS measurements, the frequency range was from 0.01 Hz to 10 kHz with $E=E_{\text{open circuit}}$.

The phase of the specimen surface was measured by X-ray diffraction (XRD, PANalytical Empyrean, Malvern Panalytical, UK) with $2\theta = 30^\circ - 65^\circ$ and step size of $2^\circ/\text{min}$. The surface morphology was observed by scanning electron microscope (SEM, MIRA LMS, TESCAN, Czech Republic). The electron backscattered diffractometer (EBSD, Hikari Plus, EDAX, USA) was used to characterize the crystal microstructure and characteristics.

2 Results and Discussion

2.1 Tafel curve

Fig.1 shows the Tafel curves of HT1, HT3, HT5, HT7, and HT9 specimens. It can be seen that HT5 and HT9 specimens have lower corrosion current densities, HT1 and HT3 specimens have similar corrosion current densities, and the corrosion current density of HT7 specimen is the largest. HT5 specimen shows the optimal corrosion resistance, whereas the HT7 specimen shows the worst corrosion resistance^[25]. The

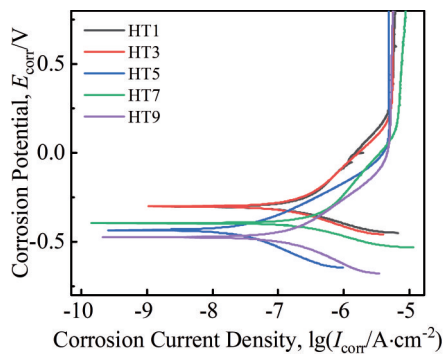


Fig.1 Tafel curves of specimens HT1, HT3, HT5, HT7, and HT9

potential at the current intersection point is denoted as the corrosion potential E_{corr} , and the corrosion current density I_{corr} can be correspondingly obtained^[26-27]. The mean value and standard deviation of corrosion potential and corrosion current density are shown in Table 1. It can be seen that the corrosion current density of different specimens can be arranged from the smallest to the largest as follows: HT5<HT9<HT3<HT1<HT7. The optimal corrosion current density is $0.037 \mu\text{A}/\text{cm}^2$, indicating that HT5 specimen has the optimal corrosion resistance.

2.2 EIS test

The corrosion mechanism was evaluated through Nyquist and Bode diagrams, as shown in Fig. 2. Fig. 2a shows the Nyquist plots of different specimens. The arc radius of different specimens can be arranged from the largest to the smallest as HT5>HT9>HT3>HT1>HT7. The larger the arc radius of the Nyquist curve, the better the corrosion resistance^[28]. Thus, the corrosion resistance of HT5 specimen is optimal, which is consistent with the Tafel curve results. Fig. 2b and 2c show the Bode plots of different specimens. At high frequencies, the $\lg|Z|$ values tend to be constant, indicating that all specimens in the solution form a protective film, namely passivation layer^[29-30]. The phase angle value gradually decreases at high frequencies, and it is close to 90° in the middle- and low-frequency regions^[31]. The stronger the protective passivation film formed on the surface, the greater the phase angle value. From this perspective of view, HT5 specimen has the strongest passivation film, indicating the optimal corrosion resistance.

Fig. 2d shows the equivalent circuit diagram based on the Nyquist plot. R_s represents the electrolyte resistance; R_p is the passivation layer resistance; CPE_1 represents the constant phase angle element; R_{ct} is the interfacial transfer resistance; CPE_2 represents the electric double layer capacitance. The constant phase element (CPE) matches the rough surface characteristics of the electrode. The relevant circuit impedance parameters are shown in Table 2. The electrolyte resistance (R_s) of different specimens is similar to each other, regardless of the specimen type and test setup, indicating the good reproducibility of the tests^[32-33]. The magnitude order of R_p and R_{ct} values of different specimens can be arranged from the largest to the smallest as HT5>HT9>HT3>HT1>HT7. The resistance of passivation layer and interface transfer resistance obviously increase. The stronger the passivation film, the

Table 1 Corrosion current densities and corrosion potentials of specimens HT1, HT3, HT5, HT7, and HT9

Specimen	Corrosion current density, $I_{\text{corr}}/\mu\text{A}\cdot\text{cm}^{-2}$	Corrosion potential, E_{corr}/V
HT1	0.245 ± 0.015	-0.335 ± 0.027
HT3	0.188 ± 0.010	-0.331 ± 0.031
HT5	0.037 ± 0.008	-0.461 ± 0.022
HT7	0.364 ± 0.013	-0.429 ± 0.037
HT9	0.143 ± 0.009	-0.481 ± 0.028

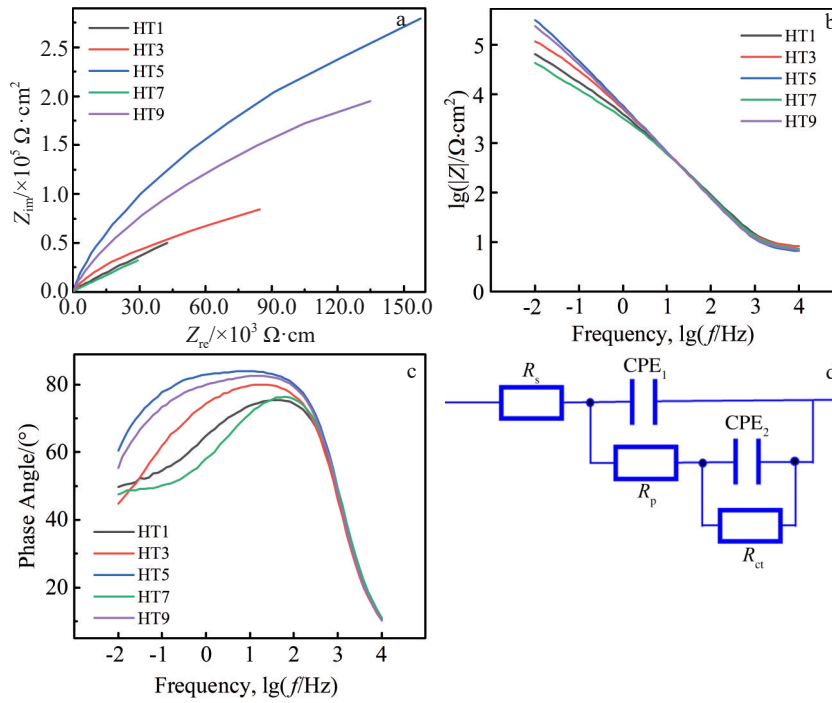


Fig.2 Nyquist diagram (a), Bode diagrams (b–c), and equivalent circuit diagram (d) of specimens HT1, HT3, HT5, HT7, and HT9

Table 2 Equivalent circuit impedance parameters of different specimens

Specimen	$R_s/\Omega \cdot \text{cm}^2$	$R_p/\Omega \cdot \text{cm}^2$	$R_{ct}/\Omega \cdot \text{cm}^2$	Error/%
HT1	7.596	12 278	158 940	3.79
HT3	7.994	16 058	512 030	2.47
HT5	6.565	157 530	912 020	2.62
HT7	6.979	4 782	114 830	3.98
HT9	6.904	55 574	632 020	2.09

greater the interface transfer resistance, and the better the corrosion resistance^[34–35]. The results all suggest that HT5 specimen has the optimal corrosion resistance, whereas HT7 specimen has the worst corrosion resistance.

2.3 Surface morphology before and after electrochemical corrosion

SEM surface morphologies of HT1, HT3, HT5, HT7, and HT9 specimens before and after electrochemical corrosion are shown in Fig. 3. The surface after the corrosion tests has obvious irregular corrosion pits and grooves, and the surface becomes rough^[36]. The corrosion degree of HT5 specimen surface is the lightest, whereas severe corrosion occurs on the surface of HT1 and HT7 specimens. This result is also consistent with the abovementioned results.

2.4 Phases of Ti6Al4V alloy

The crystal phase structures of the surface of HT1, HT3, HT5, HT7, and HT9 specimens are shown in Fig. 4. After polishing, the β -phase is bright. The specimens all show a basket microstructure with distinct titanium flakes and the microstructural fineness slightly varies^[37]. The boundary of the β -phase crystal of HT7 specimen is blurry, compared with that

of other specimens. The microstructures of all other specimens are similar. The microstructure is composed of elongated α -grain and intergranular β -grain, which shows the typical microstructure of Ti6Al4V alloy under heat treatment conditions.

XRD patterns of HT1, HT3, HT5, HT7, and HT9 specimens are shown in Fig. 5. The same phases with different intensities exist in all specimens. These specimens are mainly composed of hexagonal Ti (α) and a little β -phase (110)^[38]. According to Fig. 5, there is no obvious orientation difference between the main phase peaks of different specimens. HT1 and HT5 specimens barely have β -phase, whereas HT3, HT7, and HT9 specimens have a little β -phase.

To further investigate the differences in crystal structure, the phase composition of different specimen was measured by EBSD. Fig. 6 shows the proportion of α -phase (close-packed hexagonal-Ti, hcp-Ti) and β -phase (body-centered cubic-Ti, bcc-Ti) in HT1, HT3, HT5, HT7, and HT9 specimens. The proportion of α -phase in all specimens is obviously higher than that of β -phase. The proportion of β -phase is quite low to 0.6%, 0%, 0.1%, 0.3%, and 0.2% for the HT1, HT3, HT5, HT7, and HT9 specimens, respectively. Because of the limitation of instrument measurement, the results deviate slightly from XRD results. Since the proportion of β -phase is really low, the effect of β -phase on corrosion performance can be ignored.

2.5 Crystal structure

Inverse pole figure maps, misorientation angle maps, rotation angle maps, and grain size distributions of HT1, HT3, HT5, HT7, and HT9 specimens are shown in Fig. 7. According to the inverse pole figure maps, the crystal orientation distribution of HT5 specimen is the most uniform, and HT5 specimen mainly consists of <111> crystal orientations^[39].

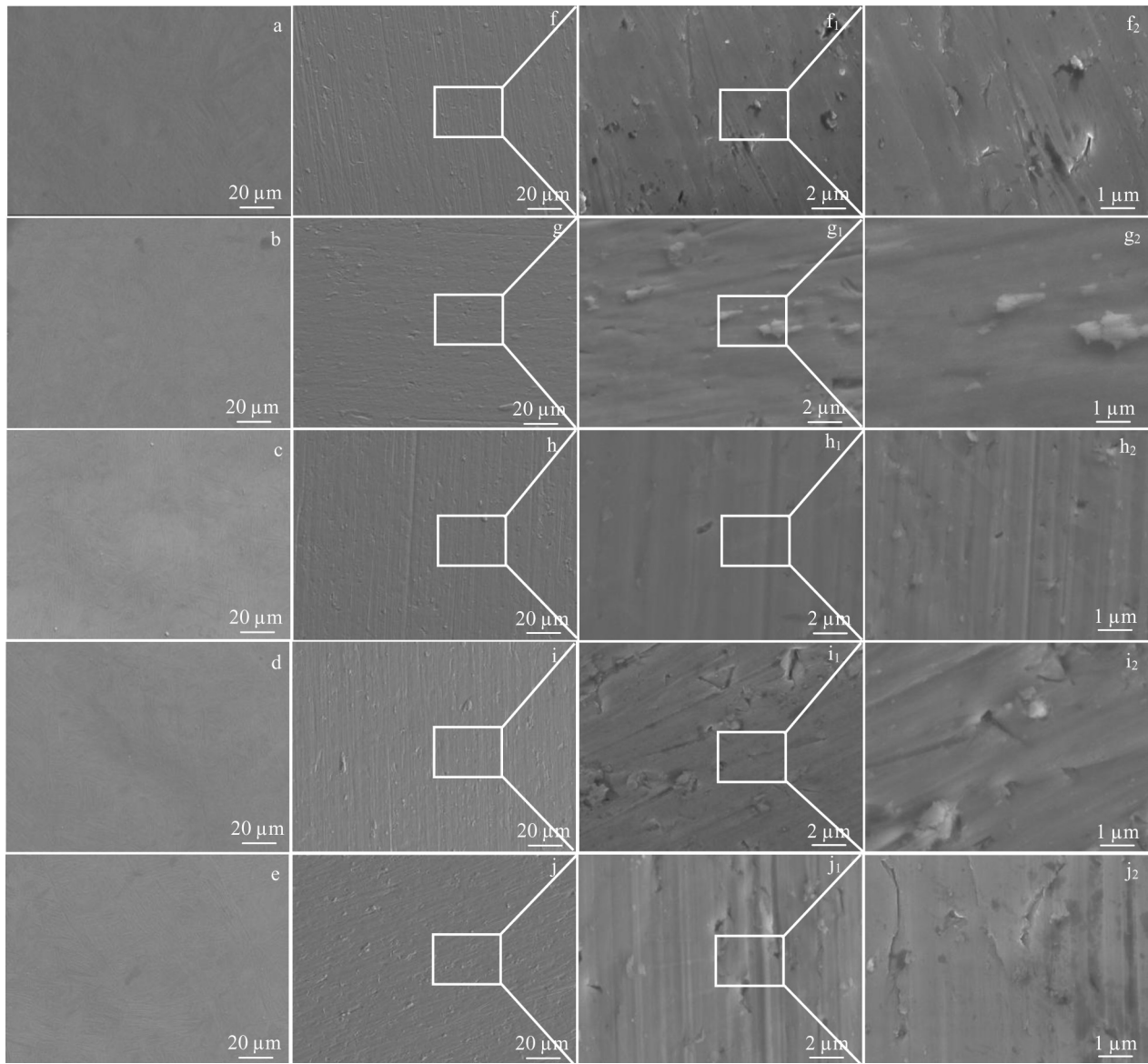


Fig.3 SEM surface morphologies of specimens HT1 (a, f, f₁-f₂), HT3 (b, g, g₁-g₂), HT5 (c, h, h₁-h₂), HT7 (d, i, i₁-i₂), and HT9 (e, j, j₁-j₂) before (a-e) and after (f-j, f₁-j₁, f₂-j₂) electrochemical corrosion

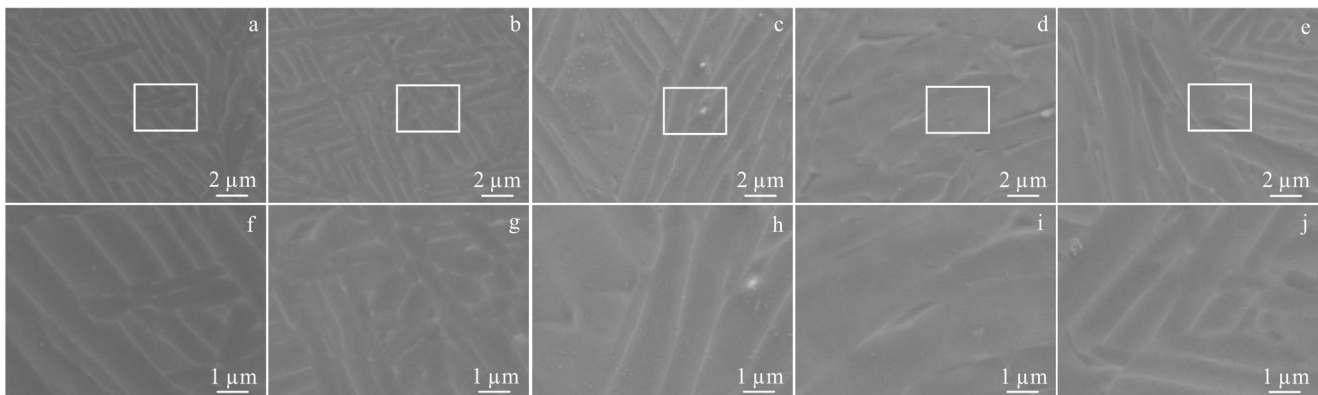


Fig.4 SEM crystal phase structures (a-e) and magnified rectangular areas (f-j) of specimens HT1 (a, f), HT3 (b, g), HT5 (c, h), HT7 (d, i), and HT9 (e, j)

There is also a trace of <001> crystal orientation. Other specimens are crystal-oriented along all directions. HT1

specimen has the most <101> crystal orientations, followed by HT7 specimen. There is no discernible change in the

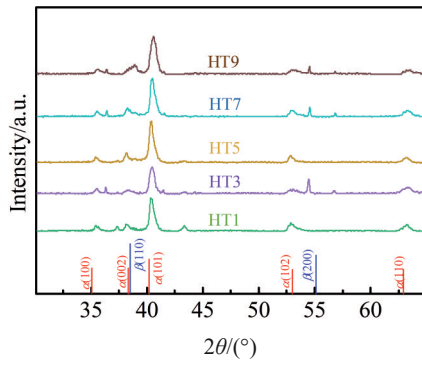


Fig.5 XRD patterns of specimens HT1, HT3, HT5, HT7, and HT9

proportion of $\langle 001 \rangle$ crystal orientation. According to the corrosion resistance results, HT5 specimen has the optimal corrosion resistance, thus inferring that the $\langle 111 \rangle$ crystal orientation possesses better corrosion resistance. With prolonging the heat treatment duration, the misorientation angle is decreased firstly and then increased. When the orientation angle is large, the grain boundary increases, leading to flaws or impurities and resulting in localized corrosion or electrochemical process. Small misorientation angles lead to strong corrosion resistance^[40]. The minimum misorientation angle is 18.61° for the HT5 specimen, and HT3 specimen has the second smallest misorientation angle.

The red lines in the rotation angle maps represent the grain

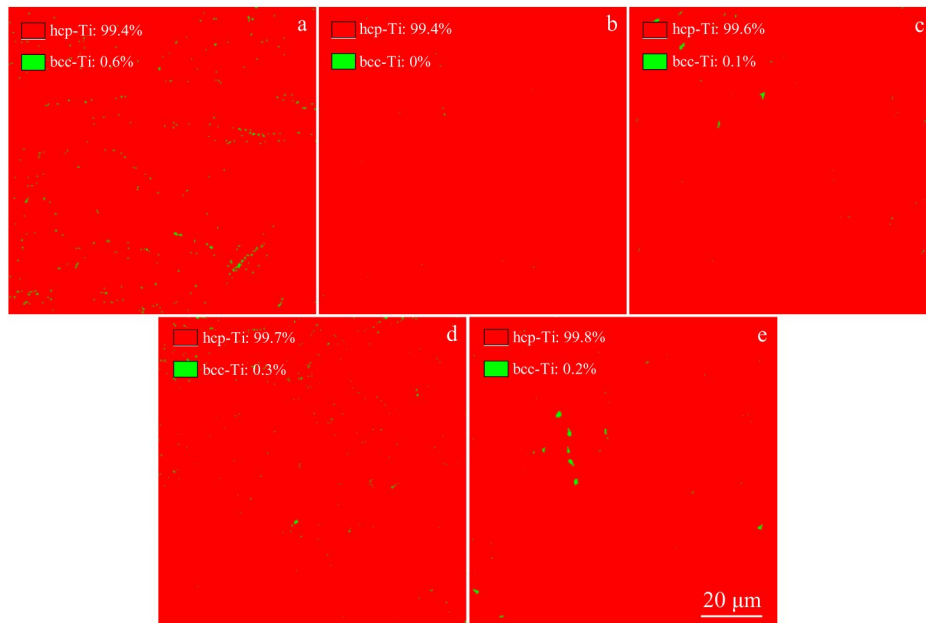


Fig.6 Proportions of α -phase and β -phase in specimens HT1 (a), HT3 (b), HT5 (c), HT7 (d), and HT9 (e)

boundaries with misorientation angle of 2° – 5° , the green lines represent the grain boundary with misorientation angle of 5° – 15° , and the blue lines represent the grain boundaries with misorientation angle over 15° . The grain boundary may become a corrosive site, and it is more likely to be corroded or electrochemically react with corrosive medium than the grain interior. Furthermore, broader grain boundaries may result in more flaws or pores, promoting the permeation of corrosive medium into the material interior^[41]. HT5 specimen contains the most small-angle grain boundaries (56.2%), indicating that HT5 specimen has the optimal corrosion resistance, followed by HT3 specimen. The grain intercept length of HT5 specimen is the largest ($5.252 \mu\text{m}$), followed by that of HT9 specimen ($4.491 \mu\text{m}$). The larger the grains, the less the grain boundaries, and the less the corrosion channels, thereby enhancing the corrosion resistance^[42]. As a result, HT5 specimen has the optimal corrosion resistance, followed by HT9 specimen from the perspective of intercept length.

Typical textures for metals with hcp crystal structure are located at $\varphi_2=0^\circ$ or $\varphi_2=30^\circ$ section. Thus, in this research, the

φ_2 section is fixed as $\varphi_2=0^\circ$ or $\varphi_2=30^\circ$ for analysis^[43]. Fig. 8 shows orientation distribution function (ODF) diagrams of the α -phase in HT1, HT3, HT5, HT7, and HT9 specimens. When $\varphi_2=0^\circ$, the two-dimensional diagram of each specimen is presented; when $\varphi_2=30^\circ$, the three-dimensional diagram is presented. The Euler angles ($\varphi_1, \Phi, \varphi_2$) and $\{hkil\} \langle uvw \rangle$ in ODF diagrams of the Bunge system are as follows.

The strong texture of HT1 specimen at $\varphi_2=0^\circ$ is $\{\bar{1}2\bar{1}4\} \langle \bar{1}007 \rangle$ texture with the Euler angle of $(90^\circ, 90^\circ, 0^\circ)$, and its intensity is 56.467. For the HT1 specimen at $\varphi_2=30^\circ$, the strong texture can be divided into $\{0001\} \langle \bar{1}0\bar{2}0 \rangle$ texture with Euler angle of $(0^\circ, 0^\circ, 30^\circ)$ and $\{0001\} \langle 0010 \rangle$ texture with Euler angle of $(60^\circ, 0^\circ, 30^\circ)$, and its intensity is 14.718. For the HT3 specimen at $\varphi_2=0^\circ$, the strong texture can be divided into $\{0001\} \langle \bar{1}0\bar{2}0 \rangle$ texture with Euler angle of $(30^\circ, 0^\circ, 0^\circ)$, $\{0001\} \langle 0010 \rangle$ texture with Euler angle of $(90^\circ, 0^\circ, 0^\circ)$, $\{\bar{1}2\bar{1}0\} \langle \bar{1}013 \rangle$ texture with Euler angle of $(35^\circ, 55^\circ, 0^\circ)$, and $\{\bar{1}2\bar{1}4\} \langle \bar{1}007 \rangle$ texture with Euler angle of $(90^\circ, 90^\circ, 0^\circ)$. The texture intensity is 50.174. At $\varphi_2=30^\circ$, the strong texture of HT3 specimen is identical to that of HT1

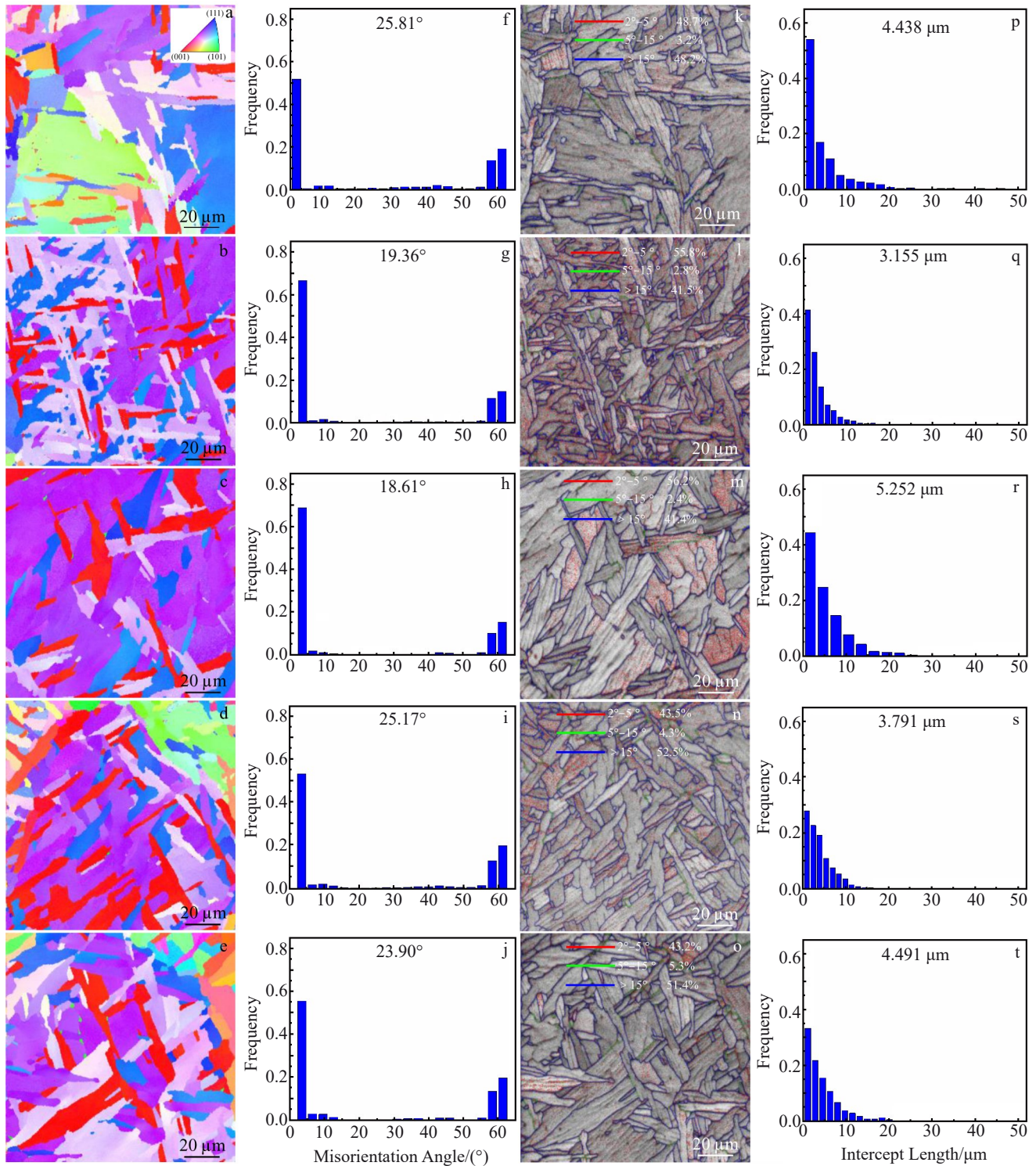


Fig.7 Inverse pole figure maps (a–e), misorientation angle distributions (f–j), rotation angle maps (k–o), and intercept length distributions (p–t) of specimens HT1 (a, f, k, p), HT3 (b, g, l, q), HT5 (c, h, m, r), HT7 (d, i, h, s), and HT9 (e, j, o, t)

specimen, but its intensity is only 50.174.

The texture distributions of HT5 specimen at $\varphi_2=0^\circ$ and $\varphi_2=30^\circ$ are similar to those of HT3 specimen, but the intensity is higher of 56.841. The texture distributions of HT7 and HT9 specimens at $\varphi_2=0^\circ$ and $\varphi_2=30^\circ$ are basically the same as those of HT3 and HT5 specimens. HT7 specimen has the highest texture intensity of 62.401, whereas the HT9 specimen has the

lowest texture intensity of 42.907. Higher texture strength leads to more constant crystal orientations, which enhances the overall corrosion resistance by homogenization of grain distributions inside the material, preventing localized corrosion and reducing the corrosion risk. Simultaneously, increasing the texture intensity can lower the tendency of directional corrosion and improve the corrosion resistance of

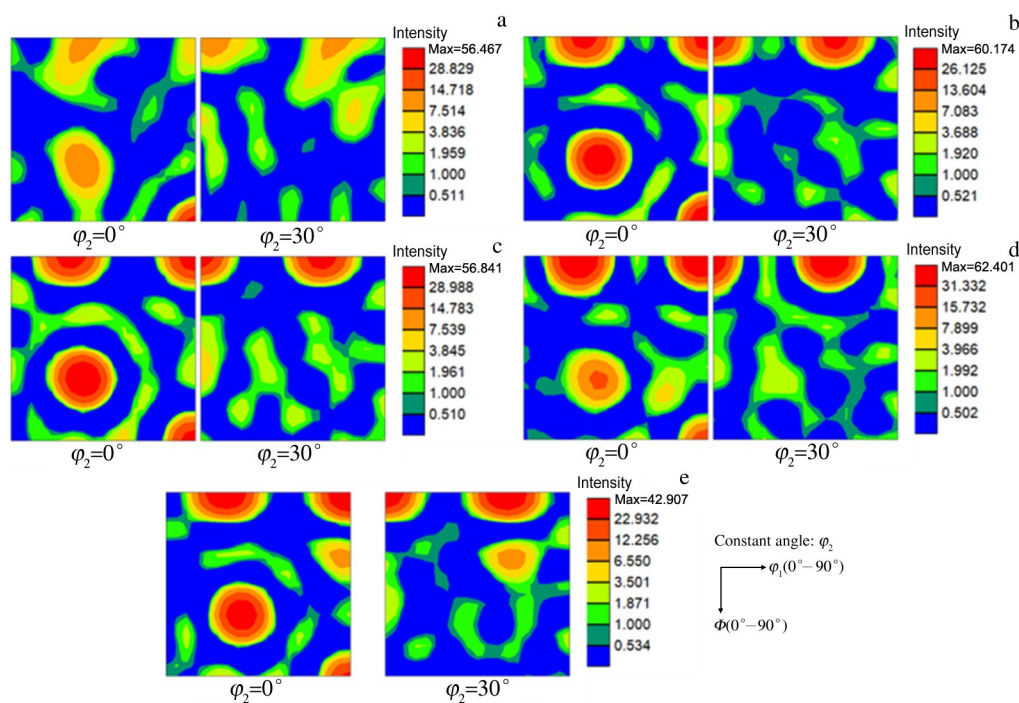


Fig.8 ODF diagrams of α -phase in specimens HT1 (a), HT3 (b), HT5 (c), HT7 (d), and HT9 (e)

materials^[44-45]. These results show that HT5 specimen has the optimal corrosion resistance, whereas HT7 specimen has the worst corrosion resistance. Additionally, it is also found that the texture intensity does not have significant influence on the corrosion performance.

3 Conclusions

1) Different heat treatment durations result in different electrochemical corrosion properties of Ti6Al4V alloys prepared by electron beam selective melting (EBSM) additive manufacturing.

2) The proportion of β -phase is very low, which can hardly influence the corrosion performance.

3) Small-angle grain boundaries can reduce corrosion degree, and large grains mean less corrosion channels.

4) The EBSMed Ti6Al4V alloy after heat treatment for 5 h has the most uniform $\langle 111 \rangle$ crystal orientation, the most small-angle grain boundaries (56.2%), the largest grain intercept length (5.252 μm), and the smallest corrosion current density (0.037 $\mu\text{A}/\text{cm}^2$), which all indicate that this specimen has the optimal corrosion resistance.

References

- 1 Kaur M, Singh K. *Materials Science and Engineering C*[J], 2019, 102: 844
- 2 Chourifa H, Bouloussa H, Migonney V et al. *Acta Biomaterialia*[J], 2019, 83: 37
- 3 Li X W, Liang J S, Shi T et al. *Ceramics International*[J], 2020, 46(9): 12911
- 4 Pervaiz S, Anwar S, Qureshi I et al. *International Journal of Precision Engineering and Manufacturing-Green Technology*[J], 2019, 6: 133
- 5 Zhang L C, Chen L Y, Wang L. *Advanced Engineering Materials*[J], 2020, 22(5): 1901258
- 6 Cai C, Gao X Y, Teng Q et al. *Materials Science and Engineering A*[J], 2021, 802: 140426
- 7 Wang J C, Liu Y J, Qin P et al. *Materials Science and Engineering A*[J], 2019, 760: 214
- 8 Gao F, Sun Z, Yang S et al. *Materials Characterization*[J], 2022, 192: 112126
- 9 Xu K, Wang M Q, Fang N W et al. *Rare Metal Materials and Engineering*[J], 2023, 52(8): 2665
- 10 Razavi S M, Van Hooreweder B, Berto F. *Additive Manufacturing*[J], 2020, 36: 101426
- 11 Schur R, Ghods S, Wisdom C et al. *Materials & Design*[J], 2021, 200: 109450
- 12 Persenot T, Burr A, Martin G et al. *International Journal of Fatigue*[J], 2019, 118: 65
- 13 Gruber H, Henriksson M, Hryha E et al. *Metallurgical and Materials Transactions A*[J], 2019, 50: 4410
- 14 Del Guercio G, Galati M, Saboori A et al. *Acta Metallurgica Sinica (English Letters)*[J], 2020, 33: 183
- 15 Knapp G L, Raghavan N, Plotkowski A et al. *Additive Manufacturing*[J], 2019, 25: 511
- 16 Lee B S, Lee H J, Lee K S et al. *Applied Surface Science*[J], 2020, 508: 145160
- 17 Montelione A, Ghods S, Schur R et al. *Additive Manufacturing*[J], 2020, 35: 101216
- 18 Li P H, Guo W G, Yuan K B et al. *Materials Characteriza-*

- tion[J], 2018, 140: 15
- 19 Del Guercio G, Galati M, Saboori A. *Metals and Materials International*[J], 2021, 27: 55
- 20 Alvi S, Neikter M, Antti M L et al. *Tribology International*[J], 2021, 153: 106 658
- 21 Kolamroudi M K, Asmael M, Ilkan M et al. *Transactions of the Indian Institute of Metals*[J], 2021, 74: 783
- 22 Qiu W B, Wei Y Q, Chen A J et al. *New Journal of Chemistry*[J], 2021, 45(6): 2967
- 23 Chern A H, Nandwana P, Yuan T et al. *International Journal of Fatigue*[J], 2019, 119: 173
- 24 Xiu M, Tan Y T, Raghavan S et al. *The International Journal of Advanced Manufacturing Technology*[J], 2022, 120(1-2): 1281
- 25 Zhou L, Deng H, Chen L et al. *Surface and Coatings Technology*[J], 2021, 414: 127096
- 26 Su B X, Wang B B, Luo L S et al. *Corrosion Science*[J], 2022, 206: 110520
- 27 Li Junfeng, Wei Zhengying, Xue Lingfeng. *Rare Metal Materials and Engineering*[J], 2023, 52(8): 2783 (in Chinese)
- 28 Zhao Y, Liu Y, Gai X et al. *Corrosion*[J], 2021, 77(8): 853
- 29 Gai X, Bai Y, Li S J et al. *Corrosion Science*[J], 2021, 181: 109258
- 30 Zhang Y F, Li J Z, Xu H Y et al. *Journal of Alloys and Compounds*[J], 2020, 849: 156622
- 31 Gai X, Liu R, Bai Y et al. *Journal of Materials Science & Technology*[J], 2022, 97: 272
- 32 Lulu-Bitton N, Sabatani E, Rosen B A et al. *International Journal of Hydrogen Energy*[J], 2022, 47(9): 6388
- 33 Yang X, Wang B, Gu W P et al. *Surface and Coatings Technology*[J], 2021, 428: 127880
- 34 Zeng C Y, Zhang Y P, Hu J L et al. *Vacuum*[J], 2020, 182: 109714
- 35 Gai X, Bai Y, Li S et al. *Acta Biomaterialia*[J], 2020, 106: 387
- 36 Kolamroudi M K, Asmael M, Ilkan M et al. *Transactions of the Indian Institute of Metals*[J], 2021, 74: 783
- 37 Lu H F, Deng W W, Luo K Y et al. *Additive Manufacturing*[J], 2023, 63: 103416
- 38 Bertolini R, Lizzul L, Pezzato L et al. *The International Journal of Advanced Manufacturing Technology*[J], 2019, 104: 2839
- 39 Wang Z R, Bai X W, Que M X et al. *Ceramics International*[J], 2023, 49(3): 4168
- 40 Cai C, Wu X, Liu W et al. *Journal of Materials Science & Technology*[J], 2020, 57: 51
- 41 Guo D, Kwok C T, Chan S L. *Surface and Coatings Technology*[J], 2019, 361: 324
- 42 Ma Z W, Shen T L, Wang Z G et al. *Applied Surface Science*[J], 2022, 578: 151910
- 43 Ji P F, Liu S G, Shi C B et al. *Journal of Alloys and Compounds*[J], 2022, 896: 163013
- 44 Wang Y S, Xiu S C, Zhang S N. *Surface and Coatings Technology*[J], 2021, 417: 127211
- 45 Bahmani A, Arthanari S, Shin K S. *Journal of Alloys and Compounds*[J], 2021, 856: 158077

热处理时间对电子束制造 Ti6Al4V 合金腐蚀性能的影响

黄俊媛, 张 伟

(北京航空航天大学 机械工程及自动化学院, 北京 100191)

摘要: 通过 1、3、5、7 和 9 h 的热处理加工电子束制备的 Ti6Al4V 样品, 进行 Tafel 和电化学阻抗谱实验, 讨论样品电化学腐蚀行为及机理。通过分析腐蚀性能的变化机理, 发现<111>晶向越多, 小角度晶界占比越大, 晶粒直径越大, 耐腐蚀性能越好。热处理 5 h 的样品呈现最均匀的<111>晶向, 小角度晶界占比最大为 56.2%, 晶粒截距 5.252 μm , 此时耐腐蚀性能最好, 腐蚀电流为 0.037 $\mu\text{A}/\text{cm}^2$ 。

关键词: Ti6Al4V; 电子束选区熔化; 耐腐蚀性能; 晶相; 晶体结构

作者简介: 黄俊媛, 女, 1993 年生, 博士生, 北京航空航天大学机械工程及自动化学院, 北京 100191, E-mail: jyhuang@buaa.edu.cn